Received: 23 November 2025 | Revised: 16 March 2026 | Accepted: 5 May 2026

DOI: 10.1002/qj.70227

Quarterly Journal of the Royal Meteorological Society RMetS

RESEARCH ARTICLE

The role of mesoscale weather effects in simulating pyroconvection: A case study of the Santa Coloma de Queralt wildfire

Koen van der Aa[1,2] | **Bernard Postema**[1,2] | **Chiel van Heerwaarden**[1] | **Tristan Roelofs**[1] | **Harm Jonker**[2,3]

[1]Meteorology and Air Quality, Wageningen University, Wageningen, the Netherlands

[2]Whiffle B.V., Delft, the Netherlands

[3]Department of Geoscience and Remote Sensing, Delft University of Technology, Delft, the Netherlands

Correspondence
Koen van der Aa, Meteorology and Air Quality, Wageningen University, Wageningen, the Netherlands.
Email: k.vanderaa@uu.nl

Present address
Koen van der Aa, Institute for Marine and Atmospheric Research in Utrecht, Utrecht University, Utrecht, the Netherlands

Funding information
EU Civil Protection Mechanism, Grant/Award Number: 101140363

Abstract

Extreme wildfire events are characterised by strong interactions between the convective wildfire plume and the atmosphere, often resulting in erratic and difficult-to-control fire behaviour. Previous (modelling) studies on pyroconvection have focused mostly on the plume's thermodynamics and induced circulation. The dynamic interactions between these convective plumes and mesoscale weather effects are less studied and are complex, due to the different scales involved. It therefore remains unclear how mesoscale effects, such as sea breezes, interact with a convective wildfire plume, and especially whether resolving mesoscale atmospheric motions is necessary to simulate wildfire plume dynamics. In this study, we present a set of large-eddy simulations (LESs), nested in a mesoscale simulation, of the Santa Coloma de Queralt wildfire in northeastern Spain (July 24, 2021). We study the interaction between a low-level moisture front and the wildfire plume and how this is dependent on the nesting of the LES, comparing our simulations with an in-plume radiosounding. We find that the LES nested in a mesoscale simulation produces a sharply defined density current of moisture, as opposed to a gradual moistening of the atmospheric boundary layer for the LES without the mesoscale nesting. This results in a different timing of pyrocumulus formation. Both LES setups produce wildfire plumes that are concurrent with the in-plume radiosounding. We also show how the front influences the circulations around the plume, resulting in a downwind rotor-like circulation. This case study therefore shows that the main added value from resolving the mesoscale explicitly is in the timing of pyrocumulus formation and circulation changes. The characteristics of the convective plume itself are not substantially different between the simulations.

KEYWORDS

large eddy simulation, mesoscale meteorology, pyroconvection, wildfire–atmosphere interactions

1 | INTRODUCTION

The frequency and intensity of wildfires have increased globally over the past decades as a result of anthropogenic climate change (Canadell *et al.*, 2021; Jones *et al.*, 2024). This trend has led to a growing number of extreme wildfire events (Cunningham *et al.*, 2024), such as the 2017 fires in Portugal (Turco *et al.*, 2019), Australia's "Black Summer Fires" of 2019/2020 (Bowman & Sharples, 2023; Nolan *et al.*, 2020), and the outbreak in California of 2025 (Barnes *et al.*, 2025). These extreme events are characterised by high fire-line intensities, resulting in strong heat-induced upward motions known as *pyroconvection* (Tedim *et al.*, 2018). Pyroconvection enhances spotting (transport of burning embers), modifies surface winds, and can ultimately lead to the formation of pyrocumulus (pyroCu) or pyrocumulonimbus (pyroCb) clouds (Finney *et al.*, 2021; Fromm *et al.*, 2022; Tedim *et al.*, 2018). Furthermore, pyroconvection is associated with increases in the rate of spread, due to the acceleration of surface rear inflow of the plume (Potter, 2012). Fire crews systematically underpredict fire behaviour (e.g., fire-line intensity and rate of spread) during extreme wildfire events because these processes are poorly understood, which leads to dangerous situations (Castellnou *et al.*, 2022).

The characteristics of pyroconvective plumes and the development of pyroCu/Cb clouds depend strongly on the atmospheric environment, specifically the thermal stratification, wind shear, and ambient moisture (Potter, 2012). The typical vertical profile associated with pyroCu/Cb formation is that of a dry, unstable mixed layer with significant moisture on top (Peterson *et al.*, 2017). Thermodynamic indices such as the lifting condensation level (LCL), convective condensation level (CCL), and convective available potential energy (CAPE) are commonly used to assess the potential for plume-induced convection (Fromm *et al.*, 2010; Lareau & Clements, 2016; Potter & Anaya, 2015). Recently, Castellnou *et al.* (2022) used radiosoundings inside wildfire plumes to classify pyroconvective behaviour based on boundary-layer stability, LCL height, and mixed-layer depth.

Due to this strong dependence of pyroconvection on atmospheric conditions, high-resolution modelling is essential to improve understanding and complement sparse observational data (Bakhshaii & Johnson, 2019). Models such as WRF-Fire (Coen *et al.*, 2013) and MESO-NH ForeFire (Filippi *et al.*, 2009) have coupled a semi-empirical fire-spread model to their main non-hydrostatic mesoscale atmospheric model. Badlan *et al.* (2021a, 2021b) and Eghdami *et al.* (2023) have, for example, investigated the sensitivity of pyroconvection to surface characteristics and atmospheric moisture content, respectively, using WRF-Fire in large-eddy simulation (LES) mode. By using MESO-NH, Filippi *et al.* (2018) and Couto *et al.* (2024) have simulated the dynamics of pyroconvective plumes. They find that these simulations resemble observed characteristics such as pyroCb formation. The modelling study by Campos *et al.* (2023) showed that a synoptic-scale storm can enhance pyroCb formation through moisture transport. This shows that modelling pyroconvection involves many relevant scales.

In this study, we focus on the influence of mesoscale atmospheric motions ($\mathcal{O}$ (2–200 km): see Markowski & Richardson, 2010) on pyroconvection. Previous studies by Badlan *et al.* (2012), Kochanski *et al.* (2013b), and Wilke *et al.* (2022) have shown how mesoscale mountain flows (particularly lee waves) can elevate local fire danger and fire spread. Furthermore, a recent high-resolution study with the Met Office Unified model by Ayat *et al.* (2025) has illustrated how mesoscale drying associated with the passing of a synoptic front elevated wildfire intensity during the 2019/2020 fires in Australia. These studies show the importance of mesoscale weather effects on wildfire behaviour, but few modelling studies have focussed specifically on the connection to pyroconvection. Furthermore, studies by van Stratum *et al.* (2023) and Postema *et al.* (2026) have shown that mesoscale features need to be resolved in atmospheric LES to model the full energy spectrum of atmospheric motions.

We therefore hypothesise that the addition of a modelling domain that resolves mesoscale atmopsheric motions (at a 2-km grid size) will impact the characteristics of simulated pyroconvection. To test this, we present LESs of a pyroconvective event that are nested in global weather data (European Centre for Medium-Range Weather Forecasts (ECMWF) Reanalysis Version 5 (ERA5)) through a nested mesoscale simulation. We study the case of the Santa Coloma de Queralt wildfire in Spain. This case study builds upon a study by Roelofs *et al.* (2026), who studied the same event using an LES with periodic boundary conditions from ERA-5 reanalysis. They showed that convective wildfire plume characteristics can be resolved using LES without a fire-spread model coupling, by comparing their simulations with an in-plume radiosounding. Such radiosoundings have been used over the past years to study the thermodynamic properties of wildfire plumes (Castellnou *et al.*, 2025), as a low-cost alternative to lidar or radar observations. In our study, we will also compare our simulation results with this in-plume radiosounding.

In addition, we have chosen to study this wildfire event because of the presence of a sharp moisture front, which likely played an important role in the formation of short-lived pyrocumulus formation (Eghdami *et al.*, 2023). The moisture front was attributed to a sea-breeze circulation by fire analysts from the Catalan fire service.[1] A sea-breeze circulation, which occurs when a pressure

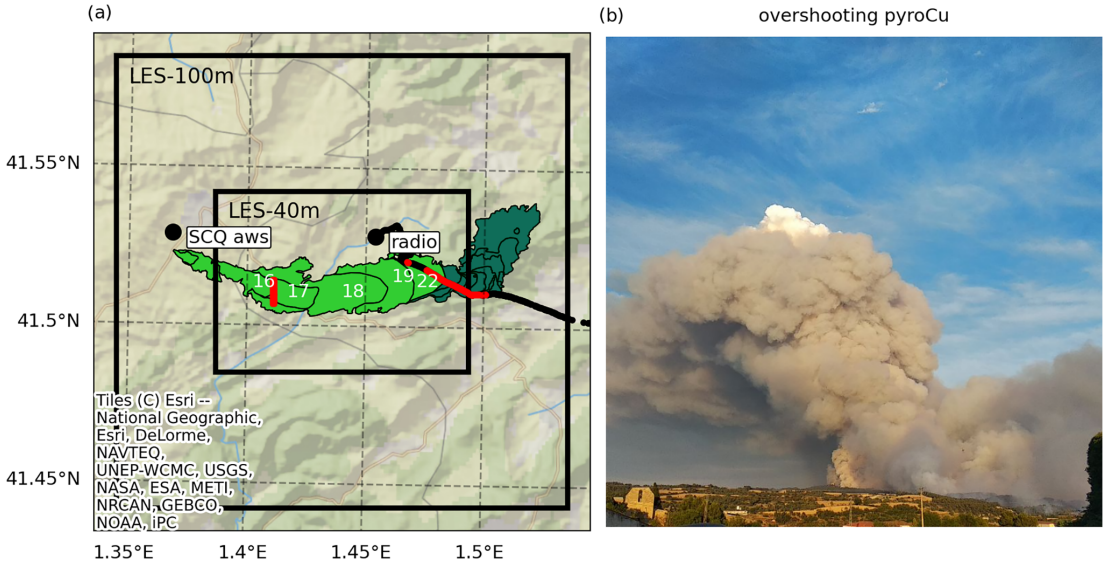

FIGURE 1 Overview of the Santa Coloma de Queralt (SCQ) wildfire event and simulation setup. (a) Burnt area per hour (light green for July 24, dark green for July 25; some of the times are indicated in hours UTC inside the isochrones) as recorded by fire analysts from the Catalan fire service for the entire wildfire event (see also Castellnou *et al.*, 2022). The locations of the SCQ automatic weather station (SCQ aws) and the radiosounding of July 24 at 1941 UTC (radio) are represented by black dots. The part of the radiosounding where its rising speed was above 2 $m \cdot s^{-1}$ is coloured red. The LES-100m and LES-40m domains are illustrated by black rectangles and annotated accordingly. The red line represents the source area of the fire heat flux within the LES-40m domain. (b) Convective wildfire plume of the SCQ wildfire on July 24 at 1826 UTC, showing overshooting pyrocumulus clouds at the top of the plume (Source: Catalan Fire and Rescue service).

gradient forms over a land–sea boundary due to differential heating, leads to a landward-propagating front that is characterised by convective motions (Miller *et al.*, 2003). Sea-breeze circulations are regularly observed in this area (Bedoya-Valestt *et al.*, 2023).

Observational studies by Hanley *et al.* (2013) and Pinto *et al.* (2022) have confirmed that such sea-breeze circulations can influence the intensity of pyroconvection. Furthermore, a modelling study by Peace *et al.* (2015) has shown that a fire, in turn, can also affect the sea-breeze circulation. Therefore, although our main objective is to characterise the influence of resolving or not resolving mesoscale atmospheric motions, a secondary objective of this study is to understand better the interaction between the moisture front and a pyroconvective plume. With this study, we aim to inform future modelling strategies on the role of mesoscale weather effects in pyroconvection and the need to resolve them accurately in simulations.

2 | DATA AND METHODOLOGY

2.1 | Case description and observations

The Santa Coloma de Queralt wildfire occurred on July 24 and 25, 2021, in northeastern Spain, approximately 70 km northwest of Barcelona. The fire started at 1400 UTC (1600 LT) close to the town of Santa Coloma de Queralt and developed upslope in an eastward direction under synoptic westerly winds (Figure 1a). On both July 24 and July 25, there was an incoming moisture front at the end of the afternoon that shifted the winds from westerly to southwesterly and brought colder temperatures and enhanced moisture. These meteorological, likely sea-breeze, phenomena coincided with two critical periods associated with moist pyroconvection. The first was on July 24, around 1830 UTC, when small pyroCu clouds were observed at the top of the plume (Figure 1b), which are classified as overshooting pyroCu in Castellnou *et al.* (2022). The second was on July 25, around 1830 UTC, when deep pyroCb clouds were observed and firefighters had to evacuate the area due to unpredictable winds. During this event, a total of 1657 ha burned and 168 civilians had to be evacuated (see also Eghdami *et al.*, 2023).

In this study, we focus on the moisture boundary of the first day (July 24), because preliminary analysis of the observations and simulations showed that the moisture boundary was more pronounced on this day. Furthermore, Roelofs *et al.* (2026) also simulated July 24, which will allow a side-by-side comparison. During the critical period of moist pyroconvection on July 24, a radiosounding was released from the flank of the fire (Figure 1a), at 1941 UTC. The radiosonde recorded altitude, pressure, temperature, relative humidity, and rising speed.[2] This radiosounding

TABLE 1 Domains and nesting strategy.

Simulation setup	Meso	LES-100m	LES-40m
Horizontal domain [km × km]	256 × 256	16 × 16	6.4 × 9
Horizontal grid size [m]	2000	100	40
Vertical domain [m]	9500	6000	6000
Vertical grid size (stretched) [m]	50–400	30–130	15–120
Duration [hours]	15	15	6.5
Start time [dd hh:mm UTC]	24 06:00	24 06:00	24 14:30
Spin-up [hours]	6	1	1
Turbulence scheme	Troen and Marht	Rozema	Rozema

and others have been presented earlier in the study by Castellnou *et al.* (2022).

2.2 | Model and numerical setup

In this study, two modelling strategies will be compared using the Atmospheric Simulation Platform for Innovation, Research, and Education (ASPIRE) model. Below, we first give a brief description of this model and then detail the setup of the simulations.

2.2.1 | ASPIRE

ASPIRE is a computational modelling tool that allows for weather forecasting using LES. The model originated from the Dutch Atmospheric Large Eddy Simulation (DALES) model (Heus *et al.*, 2010) and has been optimised to run on graphic processing units (Schalkwijk *et al.*, 2012, 2015). ASPIRE includes modules for radiation, microphysics, and land-surface interactions and runs with open boundary conditions, nested in a mesoscale simulation, also run with ASPIRE. This mesoscale simulation uses the same model formulation as the LES, different only in that all turbulence is parametrised using the non-local formulation by Troen and Mahrt (1986). In the LES, the subgrid turbulence is parametrised following Rozema *et al.* (2015). ASPIRE has been used mainly for wind forecasting and wind resource assessment (Baas *et al.*, 2023; Postema *et al.*, 2025; Schepers *et al.*, 2021), but also for, for example, dispersion (Bieringer *et al.*, 2021).

2.2.2 | Fire implementation and simulation setup

In this study, we make use of a nested simulation approach, where an LES of 6.4 km by 9 km (40-m grid size, "LES-40m") is nested in an LES of 16 km by 16 km (100-m grid size, "LES-100m") which in turn is nested in a mesoscale simulation of 256 km by 256 km (2000-m grid size); see also Figure 1 and Table 1. The boundary conditions for the outer domain (i.e., the mesoscale domain in the *base* and *base_nofire* simulations and the LES-100m domain in the *nomeso* and *nomeso_nofire* simulations) are updated every time step, based on linearly interpolated hourly ERA-5 reanalysis fields (Hersbach *et al.*, 2020). The boundary conditions for the nested simulations are also updated each time step. The simulations are centred around the middle of the LES-40m domain. The mesoscale simulations include a spin-up time of 6 hours, and the LES a spin-up time of 1 hour.

To produce the convective plumes associated with the observed wildfires, we add a collection of point sources producing a constant heat flux in the LES-40m domain over an area of 920 m by 120 m (see Figure 1). This area was chosen based on the reported flaming-zone depth of 150 m (Roelofs *et al.*, 2026) and the width of the isochrones. The point sources produce a constant heat flux of 272 MW per grid cell, which is equal to 170 $\mathrm{kW \cdot m^{-2}}$. This heat flux is based on Roelofs *et al.* (2026), who determined it to be between 120 and 170 $\mathrm{kW \cdot m^{-2}}$ based on the fire-line intensity equation (Byram, 1959). The heat flux in this study thus reflects the upper end of this range and therefore the most intense pyroconvection. Next to the heat flux, an inert tracer is released at the source to visualise the smoke-plume trajectory. Preliminary simulations indicated that these point sources had to be implemented approximately 50 m above the ground level, so as not to disturb the surface energy balance scheme. Similar to Roelofs *et al.* (2026) and Badlan *et al.* (2021a), the interaction of the fire with the surface is not considered, meaning neither the wildfire spread nor the changes in intensity are simulated. Although this limits to a certain extent the realism of the simulation, it also provides a more confined setup in which we can focus solely on the atmospheric processes. The assumption of a stationary front instead of a moving

TABLE 2 Simulations.

Simulation	Nesting	BC[a] outer nest	Fire size [m × m]	Fire intensity [kW · m^{-2}]
base	meso/LES-100m/LES-40m	ERA-5	120 × 920	170
base_nofire	meso/LES-100m/LES-40m	ERA-5	N.A.	N.A.
nomeso	LES-100m/LES-40m	ERA-5	120 × 920	170
nomeso_nofire	LES-100m/LES-40m	ERA-5	N.A.	N.A.

[a]BC = boundary condition.

front can be justified by the fact that the rate of spread is significantly lower (approximately 1 m · s^{-1}, according to the analysis by the Catalan fire service) than the average horizontal wind speed (5 m · s^{-1}). Furthermore, the assumption of a (constant) linear fire line is often made to simplify the firefront (Finney *et al.*, 2021). We assume that the curvature of the fire front is negligible due to the size of the fire. Badlan *et al.* (2021b) have shown that, for aspect ratios smaller than 1:16, there is little difference in plume characteristics between rectangular and circular sources.

To study the effect that the wildfire plume has on its environment, we consider two simulations: one with the fire heat source implemented and one without, called *base* and *base_nofire*, respectively. The difference between these two simulations gives the effect of the convective plume on the local atmospheric circulation. To study the impact of the mesoscale representation, we also run these simulations without the mesoscale model, which we will refer to as *nomeso* and *nomeso_nofire*. In these simulations, the boundary conditions from the LES-100m domain come directly from the ERA-5 reanalysis data. The four simulations are listed in Table 2. The 3D simulation output consists of 15-minute averages, while the output of the horizontal terrain-following slices consists of 10-minute averages.

3 | RESULTS

3.1 | Simulated weather conditions

The meteorological conditions around Santa Coloma de Queralt (SCQ) during the fire period were influenced by a complex synoptic and mesoscale situation. In this section, we first describe the observations of the SCQ weather station and how the *base_nofire* and *nomeso_nofire* simulations compare. Then we discuss our interpretation of the meteorological situation.

Figure 2 shows the observed temperature (Figure 2a), specific humidity (Figure 2b), wind speed (Figure 2c), and wind direction (Figure 2d) with black crosses. The day is characterised by high temperatures, low humidity, and moderate wind speeds. Our main interest is in the sudden rise in humidity around 1900 UTC, which the fire analysts of the Catalan Fire and Rescue Service attributed to a sea-breeze front. This increase in humidity is accompanied by an enhanced decrease in temperature and a slightly backing winds (turning counterclockwise, in this case turning to southerly). A jump in humidity accompanied by backing winds is characteristic of a sea breeze (Miller *et al.*, 2003), although not exclusive to it.

When comparing the output of the LES-40m domain at the SCQ weather station location for the *base_nofire* (blue) and *nomeso_nofire* (red) simulations, we see similarly good agreement for temperature (Figure 2a), but a substantial difference in specific humidity (Figure 2b). The *base_nofire* simulation produces a rapid increase, while the *nomeso_nofire* simulation produces a more gradual increase. Both simulations produce this increase too early compared with the observations. Furthermore, the wind speeds of the two simulations (Figure 2c) are comparable, except for the last two hours, where the *nomeso_nofire* simulation remains too high. Lastly, the wind direction of the *nomeso_nofire* simulation turns substantially from 1600 UTC onwards, deviating from the observations. The change in wind direction in the *base_nofire* simulation is also too strong, but closer to the observations.

Figure 3 compares the vertical profiles in the LES-40m domain at different times in the simulation, associated with the passing of the front indicated above. Figure 3a–c shows the domain-averaged profiles for the *base_nofire* simulation, while Figure 3d–f shows the domain-averaged profiles for the *nomeso_nofire* simulation. When interpreting these profiles, we have to keep in mind that two processes are occurring at the same time: the passing of a front and the transition from day to night. Figure 3a shows the potential temperature profiles of the *base* simulation over time, illustrating the transition from a deep mixed layer (approximately 2500 m) in blue to a stable layer (0–500 m) with a residual layer on top (500–1800 m) in green. During this transition, the specific humidity increases from 6 to 15 g · kg^{-1} and the wind backs (turns counterclockwise) in the lowest kilometre of the domain (Figure 3b,c). These profiles show that the front was rather shallow (approximately 1 km deep), which is characteristic of a sea-breeze front (Miller *et al.*, 2003).

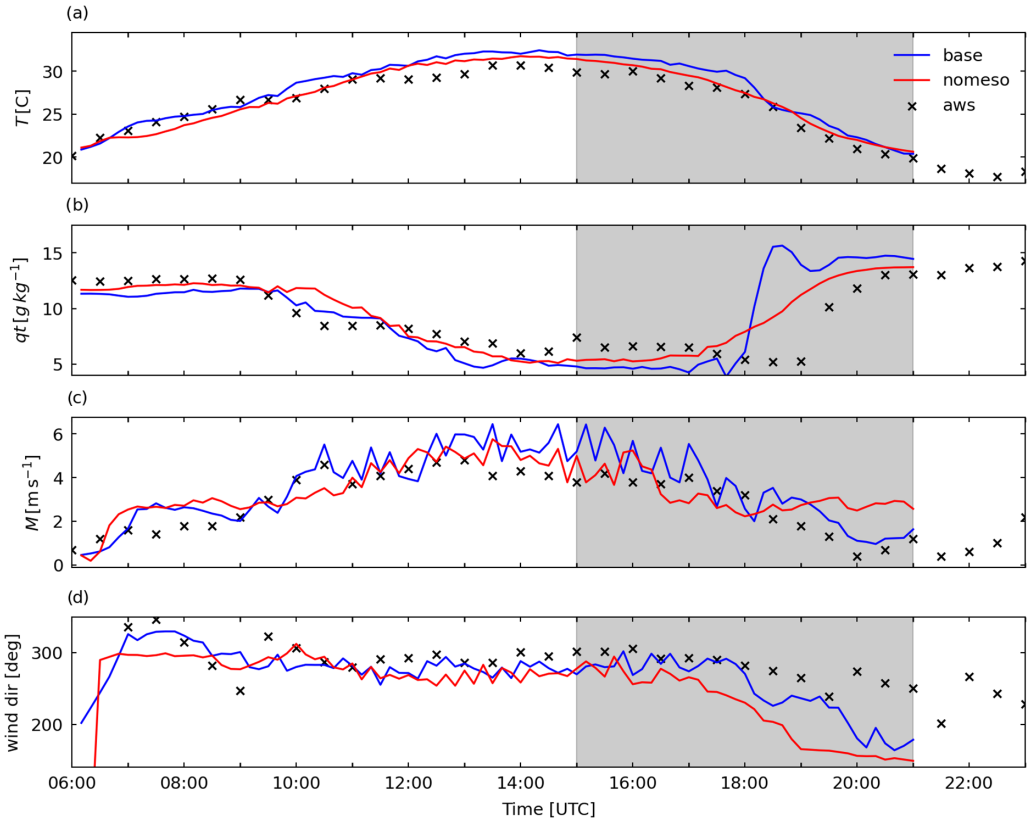

FIGURE 2 Time evolution of weather variables at Santa Coloma de Queralt (SCQ): (a) temperature T; (b) specific humidity qt; (c) wind speed M; (d) wind direction. We compare the output of the LES-100m domain simulation for the *base_nofire* (blue line) and *nomeso_nofire* line (red line) simulations at 10-m AGL with the observation of the SCQ automatic weather station (black x). The grey shading indicates the simulation period of LES-40m.

In comparison, the *nomeso* simulation produces a similar evolution of these profiles, but with important differences. First, the top of the mixed layer, as shown in the θ profiles, remains the same during the *nomeso* simulation (Figure 3d), as opposed to the lowering we see for the *base* simulation. This mixed (or boundary) layer height strongly influences wildfire plume rise, as this is limited by the stable stratification in the free troposphere (Sofiev *et al.*, 2012). We will come back to this point in the next section. Second, the qt (Figure 3e) and wind direction (Figure 3f) profiles of the *nomeso* simulation have a less clear boundary between the moist front and the drier atmosphere above. This is in line with the more gradual increase in qt we noted in Figure 2b.

This analysis shows that both simulations produce a similar evolution of a shallow front of enhanced moisture and backing wind. However, the *base_nofire* simulation shows a more defined structure, leading to a sharp increase in moisture as the front passes, instead of a gradual increase. In the next section, we will discuss how this impacts the simulated wildfire plume.

First, we have a closer look at the synoptic situation (Figure 4) and discuss whether a sea-breeze circulation had formed here. On July 23, one day before the fire, (independent) analysis by the Royal Dutch Meteorological Institute (KNMI) shows the passing of a cold front on that day. On July 24, no clear fronts are indicated by the KNMI. Figure 4a shows the contours of geopotential height (Φ/g) at 500 hPa and the geostrophic wind $V_g(= \mathbf{k} \times \frac{1}{f}\nabla_p\Phi)$ at 850 hPa, which identifies regions of stronger synoptic forcing (higher V_g; see Bedoya-Valestt *et al.*, 2023), at 1800 UTC. Figure 4b shows the potential temperature and wind at 850 hPa. These figures illustrate a low-pressure system south of the United Kingdom and a ridge of warmer air with its axis crossing the north of Italy. The westerly winds during most of the day (Figure 2d) align with the 500-hPa geopotential height contours. The apparent decrease in synoptic activity makes the interpretation of the front as a sea breeze more likely.

The meteorological situation is thus characterised by a complex synoptic situation, where a moisture front was advected over our study area during the time of the fire. This moisture front is linked to a synoptic forcing, but also resembles the characteristics of a sea-breeze front, which cannot be completely disentangled. This complex situation provides a good case study to test our hypothesis

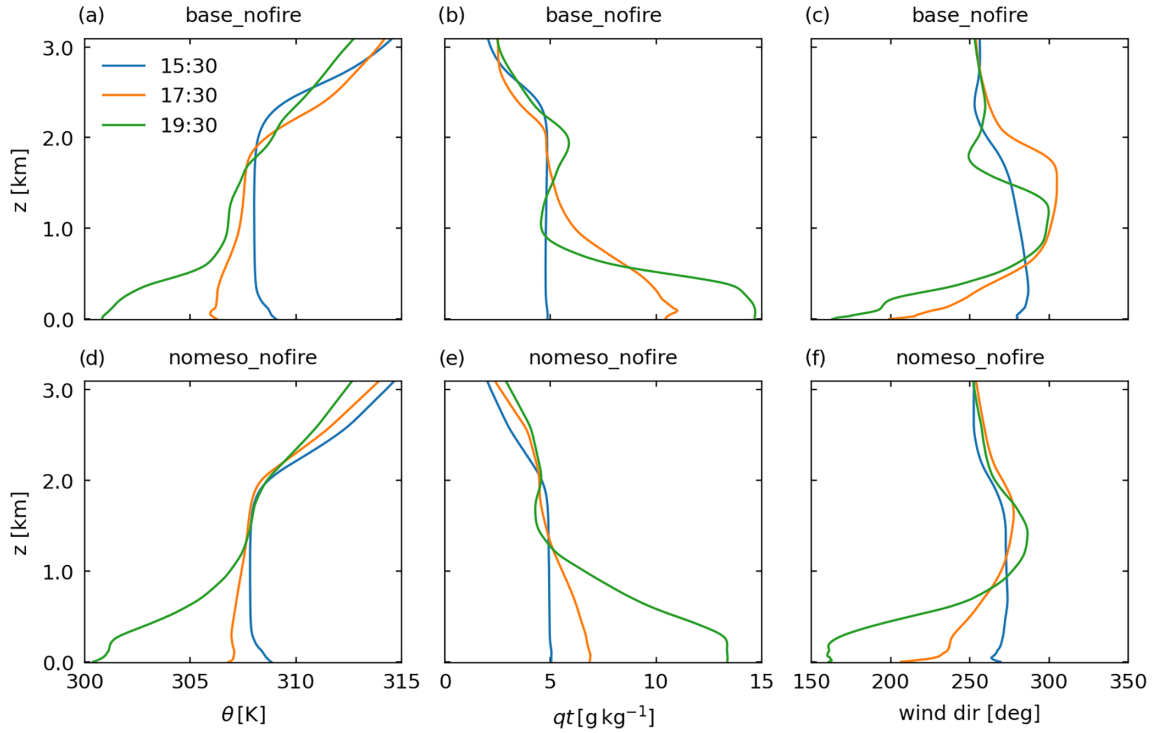

FIGURE 3 LES-40m domain-averaged vertical profiles for the *base_nofire* simulation at 1530 (blue line), 1730 (orange line), and 1930 UTC (green line), of (a) potential temperature θ; (b) specific humidity qt; (c) wind direction. (d–f) Same as (a–c), but for the *nomeso_nofire* simulation.

that resolving mesoscale atmospheric motions will influence the modelled pyroconvection. Figure 4c,d shows the near-surface potential temperature at 1800 UTC for ERA-5 and our meso model respectively. This shows that both reproduce a front advancing landward from the sea, but at different horizontal resolutions. Due to the higher resolution of the meso model, a much sharper boundary is simulated and consequently fed to the LES-100m domain, explaining the differences observed between the *base_nofire* and *nomeso_nofire* simulation above. In the next section, we discuss how this affects the simulated pyroconvection.

3.2 | Interaction between the moisture front and the convective plume

Figure 5a shows a 3D volume render of the wildfire plume in ASPIRE for the *base* simulation, where the yellow to black shading represents the concentration of the inert tracer and the green shading the local orography. Figure 5b,c shows, respectively, instantaneous horizontal and zonal cross-sections of virtual potential temperature. The instantaneous horizontal cross-section shows the location of the heat source through the enhanced temperature in red shading, as well as the arrival of the front in dark blue shading. The instantaneous zonal cross-section illustrates how the heat flux generates a plume that is warmer than its surroundings, leading to plume rise through the atmospheric boundary layer. This rise is limited by the stable stratification in the free troposphere (as shown in Figure 3), which causes the plume to spread out laterally.

Figure 6 shows the time evolution of moisture (shaded) in combination with the vertical velocity (solid contours) in the LES-40m domain for the *base* (Figure 6a–c) and *nomeso* (6d–f) simulations. The main wind direction is westerly (see Figure 3) and these (meridional) cross-sections span from south (left) to north (right). This means the vertical velocity contours in the middle of the domain display the width of the plume blowing to the east and the enhanced moisture from the front can be seen entering from the south in the *base* simulation (Figure 6a). The cross-sections are spatially averaged over the area shown in the zonal cross-sections in Appendix A.

Figure 6a–c shows how the front of enhanced moisture and vertical velocity flows through the domain like a density current, that is, a flow of a dense fluid through a lighter fluid. Once the front reaches the plume (Figure 6b), it rises more steeply and with higher updraft velocities. Furthermore, the moisture from this density current is transported upward through the plume. Consequently, water condenses to form clouds on top of the plume (dashed contour), resembling the overshooting pyroCu clouds that

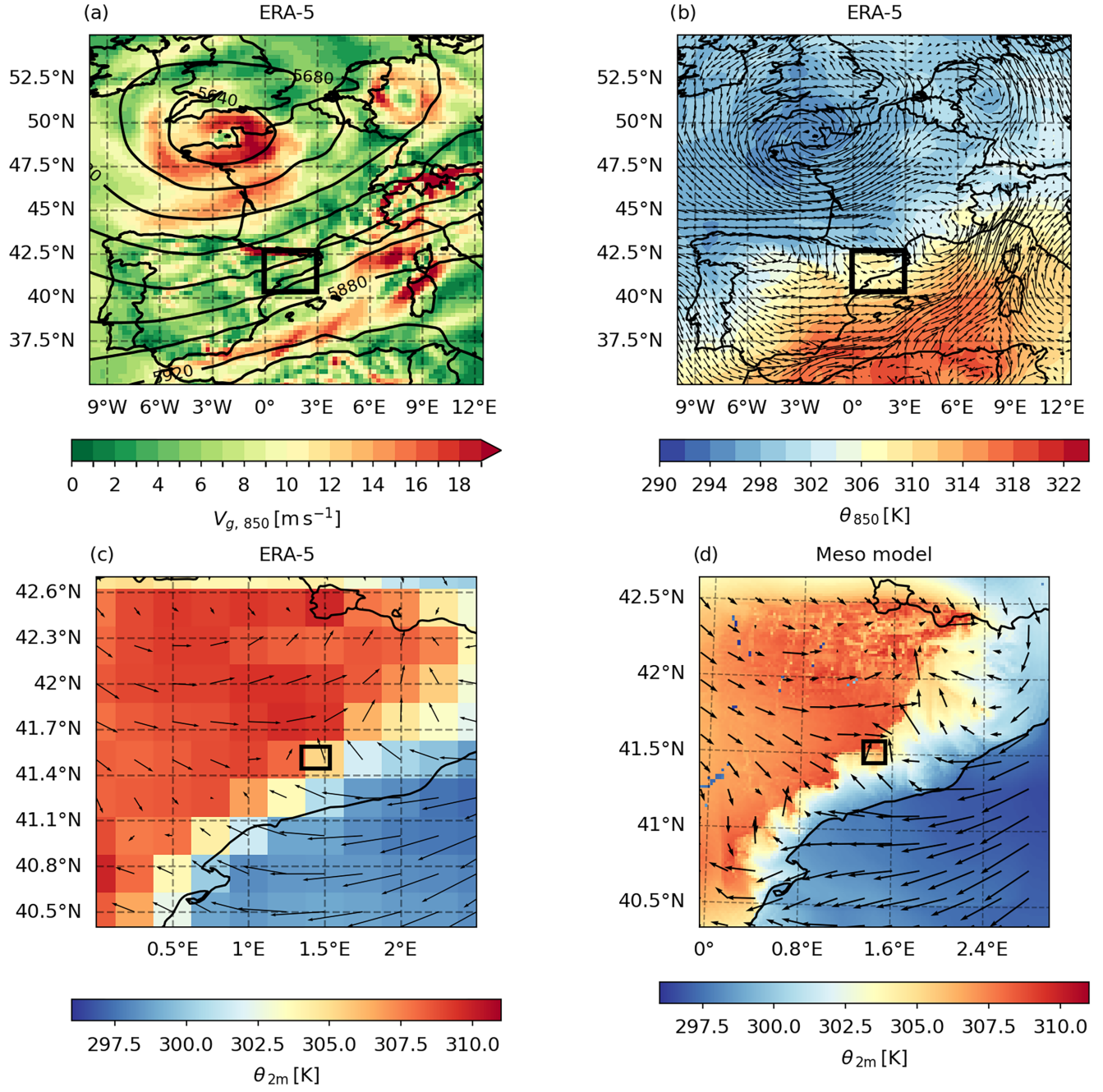

FIGURE 4 Overview of the synoptic and mesoscale situation on July 24, 1800 UTC: (a) geostrophic wind speed V_g in m · s^{-1} (shaded) at 850 hPa and geopotential height (contours) at 500 hPa based on ERA-5 reanalysis. (b) Potential temperature θ in K (shaded) and wind (arrows) at 850 hPa over Europe based on ERA-5 reanalysis. (c) Potential temperature θ in K (shaded) at 2 m above ground level and wind (arrows) at 10 m above ground level for the mesoscale domain based on ERA-5 reanalysis. (d) Same as in (c), but based on the output from the meso simulation of ASPIRE.

were observed during this event (Figure 1b). Figure 6c shows that, some time after the front has passed, a layer of strongly enhanced moisture forms at the surface, of which we saw the matching profile in Figure 3b. These three panels show how a moisture boundary, acting like a density current, interacts with the convective plume.

In contrast, Figure 6d–f does not show a density current-like front, but rather a gradual moistening of the boundary layer, concurrent with Figure 2b. The plume rises more steeply over time, as seen by the height of the vertical velocity contours (Figure 6e), similar to the *base* simulation. Cloud formation in the *nomeso* simulation

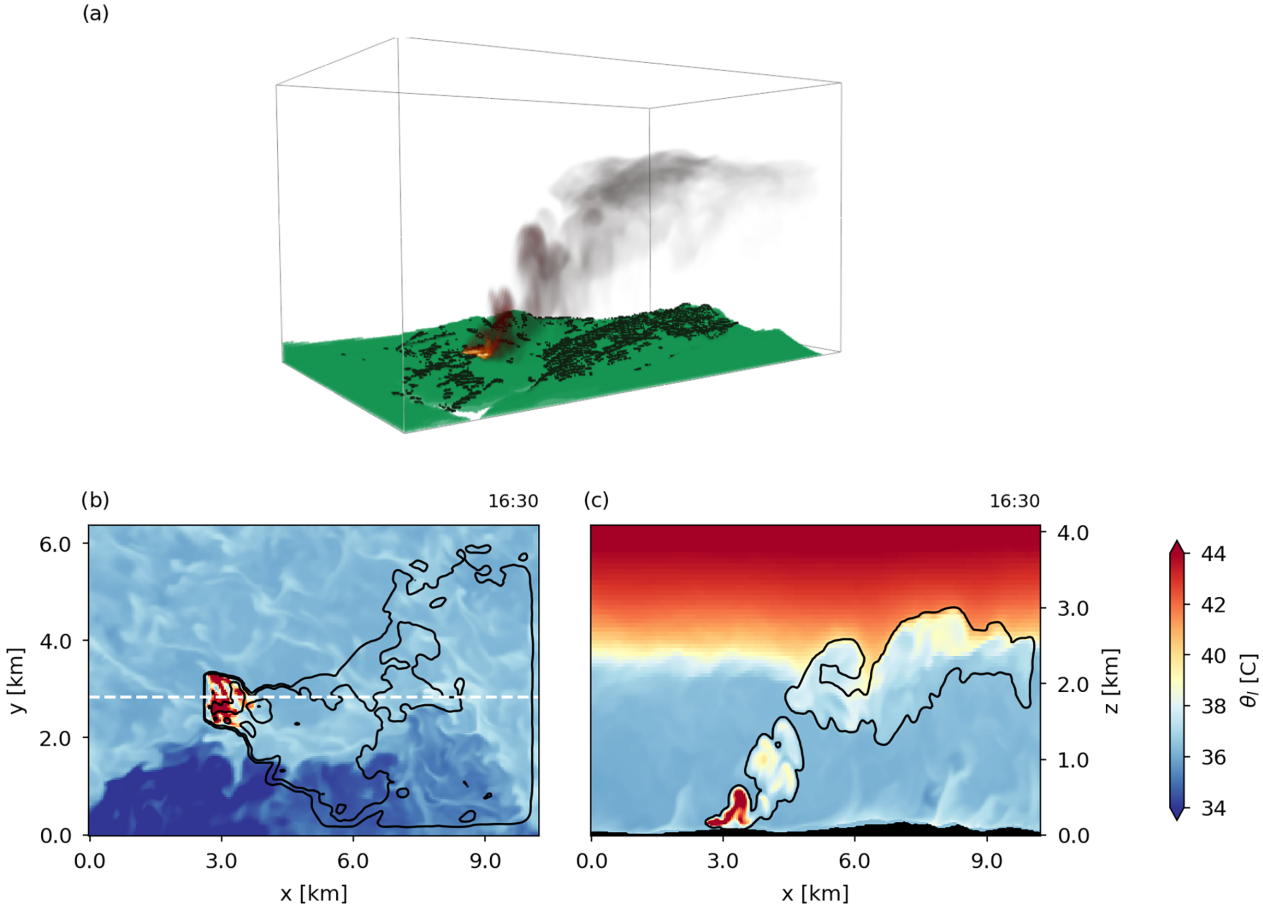

FIGURE 5 Pyroconvection in ASPIRE (*base* simulation) at 1630 UTC: (a) 3D render of the smoke concentration (yellow to black) and orography (light green represents the surface, dark green represents trees). (b) Instantaneous horizontal cross-section of temperature based on moist static energy (MSE) $\theta_l = MSE/c_p - 273.15$ (shaded) at 100 m above ground level in °C; contour lines (black) of the height-integrated concentration of the passive tracer released with the fire; the white dashed line shows the location of the vertical cross-section. (c) Zonal vertical cross-section of θ_l (shaded) and the inert tracer concentration (black contour).

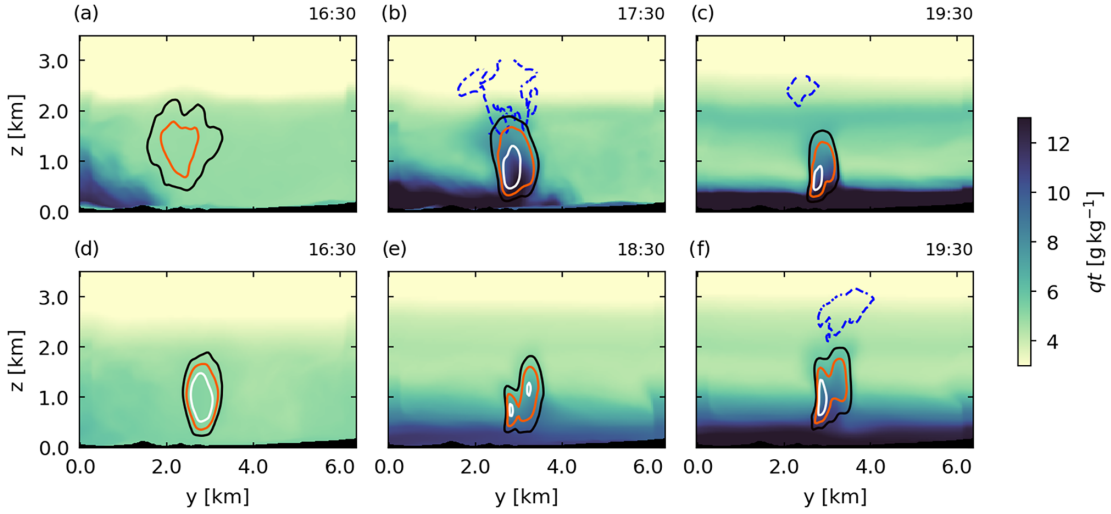

FIGURE 6 Meridional (yz) cross-sections of the *base* simulation (LES-40m) of specific humidity qt (shaded), vertical wind speed (shaded contours, $w = 2, 4, 6$ m · s^{-1}), and cloud water (dashed contour, $ql = 5 \times 10^{-5}$ kg · kg^{-1}) at (a) 1630, (b) 1730, and (c) 1930 UTC. (d–f) Same as in (a–c), but for the *nomeso* simulation at 1630, 1830, and 1930 UTC, respectively. The cross-sections are temporally averaged over the area indicated by the vertical dashed lines in Appendix A, based on the maximum w of the plume. The cloud contours are based on a meridional average for the entire domain.

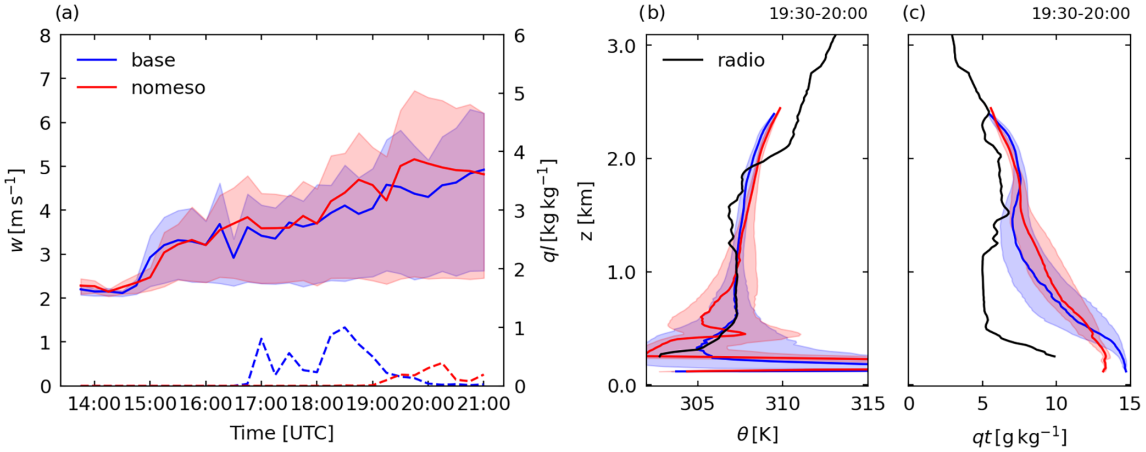

FIGURE 7 Comparison of the plume characteristics of the *base* (blue) and *nomeso* (red) simulations. The plume is defined as everywhere where $w > 2\ \mathrm{m \cdot s^{-1}}$. (a) Time evolution of median vertical velocity w inside the plume between 0 and 1.5 km (solid lines), the corresponding interquartile range (shaded), and the total liquid water content ql (dashed). (b) Vertical profile of median potential temperature θ (solid lines), the corresponding interquartile ranges (shaded), and the radiosounding launched at 1941 UTC (black line). (c) Same as (b), but for specific humidity qt.

(Figure 6f) occurs only when the boundary layer has moistened to the same level as the density current in the *base* simulation (Figure 6b). This comparison shows the difference in physical representation of the moisture front between the *base* and *nomeso* simulations: a density current bringing a clearly defined boundary, as opposed to a gradual moistening of the boundary layer.

The role of atmospheric moisture in the formation of pyrocumulus clouds had previously been established for the SCQ case by Eghdami *et al.* (2023). Through sensitivity analyses, they showed that atmospheric moisture was more important than fuel moisture, in line with earlier work such as that of Luderer *et al.* (2009) and Lareau and Clements (2016). Our results of July 24 show that the passage of the front has likely been responsible for supplying this moisture necessary for the observed overshooting pyroCu to form.

In addition, our results align with previous work on sea-breeze fronts and wildfires. For example, observations by Hanley *et al.* (2013) show that radar reflectivity, that is, intensity, of a wildfire plume increases temporarily as a sea-breeze front passes. Furthermore, idealised large eddy simulations by Cunningham (2007) show that the updraft velocity in buoyant plumes increases in response to density currents across a wide range of parameters. Specifically, he shows that this intensification occurs when the ambient wind is directed opposite to the direction of the sea breeze. Moreover, Peace *et al.* (2015) provide coupled atmosphere–fire simulations of a case study in which a sea breeze altered the wind patterns around the plume, such that a vortex-like structure developed ahead of the fire front.

It is also worth noting that this process leads to a different, but not contradictory, vertical structure conducive to pyrocumulus formation from the one suggested by Peterson *et al.* (2017), that is, a dry mixed layer with moisture on top. However, our simulation misses the effect of the moisture on the fuels, which would eventually counteract the increased buoyancy from the moisture front and cloud formation by decreasing the heat flux. The enhancing or diminishing effects of the moisture are likely dependent on the time-scale. On short time-scales, the enhancing effect will likely dominate, because the fuel does not respond instantly to the moisture, whereas the atmosphere does. On longer time-scales, the fire will likely decrease in strength due to its moistening. The fact that pyrocumulus clouds were observed during the fire gives confidence that the enhancing effect did occur, but we cannot determine how long it lasted for, due to our setup.

3.3 | Comparison with in-plume soundings

The temporal evolution of the plume's median vertical velocity and total liquid cloud water for *base* and *nomeso* is shown in Figure 7a. Here we see that the *base* simulation produces liquid cloud water above $1\ \mathrm{g \cdot kg^{-1}}$ between 1700 and 1900 UTC, when the front passes. The *nomeso* simulation produces a lower amount of cloud liquid water (maximum $0.5\ \mathrm{g \cdot kg^{-1}}$) when the boundary layer has moistened around 2000 UTC. In both *nofire* simulations, no cloud water is present. The time evolution of the median vertical velocity in the plume shows a similar behaviour for both

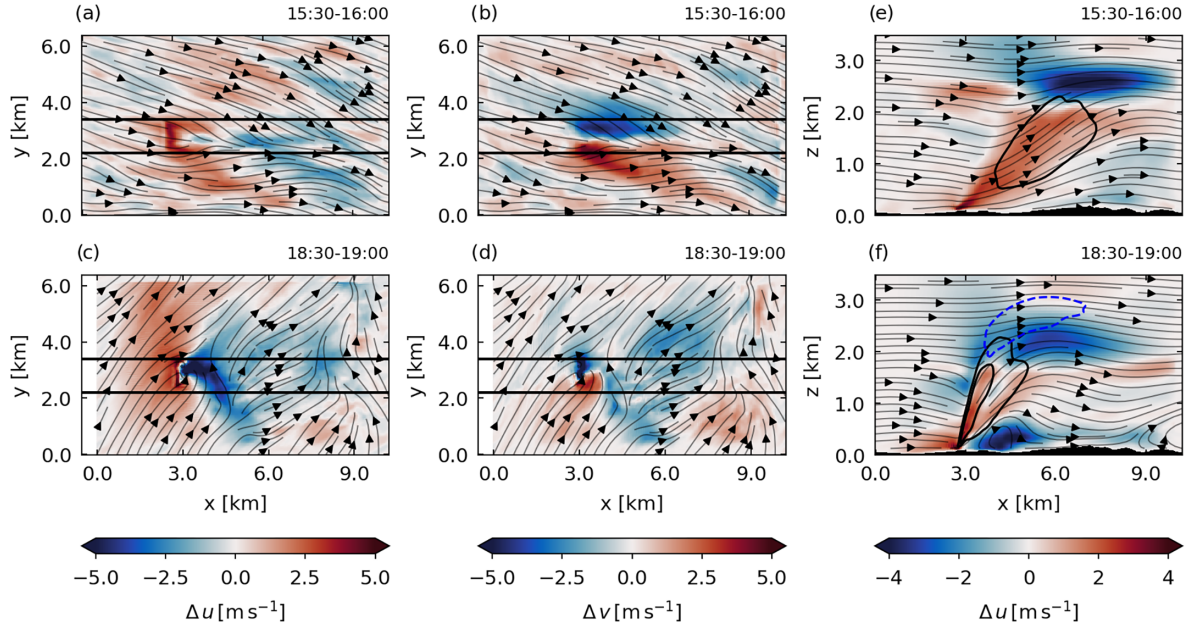

FIGURE 8 Cross-sections of the difference Δ between the *base* and *base_nofire* simulations. (a) Horizontal (*xy*) cross-section at 100 m above ground level, showing the horizontal flow field (black flow lines) and the difference in zonal velocity Δu, averaged between 1530 and 1600 UTC. (b) Same as (a), but now for the difference in meridional velocity Δv. (c,d) Same as (a,b) respectively, but now averaged over the period 1830–1900 UTC. (e) Zonal (*xz*) cross-section showing the zonal flow field (black flow lines) and the difference in zonal velocity Δu (shaded), averaged between 1530 and 1600 UTC. (f) Same as (e), but now averaged over the period 1830–1900 UTC. The zonal cross-sections are spatially averaged over the width of the source, that is, between the horizontal black lines. Cloud water is given by the dashed blue contour at $ql = 5 \times 10^{-5}$ kg · kg^{-1}.

simulations, with *w* increasing over time. This shows that the vertical velocity does not seem related to the amount of moisture or cloud formation of the front. We will explore this further in the next section on the wind field.

First, we compare the vertical profiles of potential temperature θ and specific humidity *qt* for simulations with the observations of the radiosonde launched near the plume at 1941 UTC (Figure 7b,c). The plume is defined as the area where $w > 2$ m · s^{-1} (Appendix B shows the sensitivity of the results discussed below to this threshold). Figure 7b shows the θ profile as measured by the radiosonde in black, with a mixed layer between 200 and 2000 m. The *base* simulation results in a similar profile, with magnitudes that are close to the observed values. However, we do not see a clear temperature jump between the mixed layer and the free troposphere, as is present in the observations. The *nomeso* profile does not show a clear mixed layer, but is still close to the observations in terms of magnitude.

The vertical profiles of specific humidity *qt* are similar at this time (1930–2000 UTC), but both differ markedly from the observed profile. The moisture of the lower part of the boundary layer is distributed to higher altitudes, producing a moist column. Given that the moisture front and the moistening of the boundary layer are simulated too early (Figure 2b), the moistening of the plume is also simulated too early. Likely, the plume at SCQ moistened later in the evening, but this has not been measured directly.

Using the 2 m · s^{-1} cut-off value to define the plume, we can define the plume height as approximately 1.5 km for the observations and a little under 2.5 km for the simulations. Roelofs *et al.* (2026) had similar results. This overestimation of the plume height could be attributed to the representation of the atmospheric boundary layer in the simulations. Figure 3a,d showed the thermodynamic profiles of the mixed layer, with only a weak temperature inversion for both simulations. Although the mixed layer height lowers over time in the *base* simulation, this does not influence the wildfire plume height.

Overall, the characteristics of the wildfire plumes do not differ substantially between the *base* and *nomeso* simulations when compared with the in-plume radiosounding. However, the very low number of these observations (i.e., one) limits a more thorough quantitative comparison.

3.4 | Changes in the wind field

To explore further the difference between the wildfire plumes in the simulations with and without the mesoscale model, we take a closer look at the wind fields. We

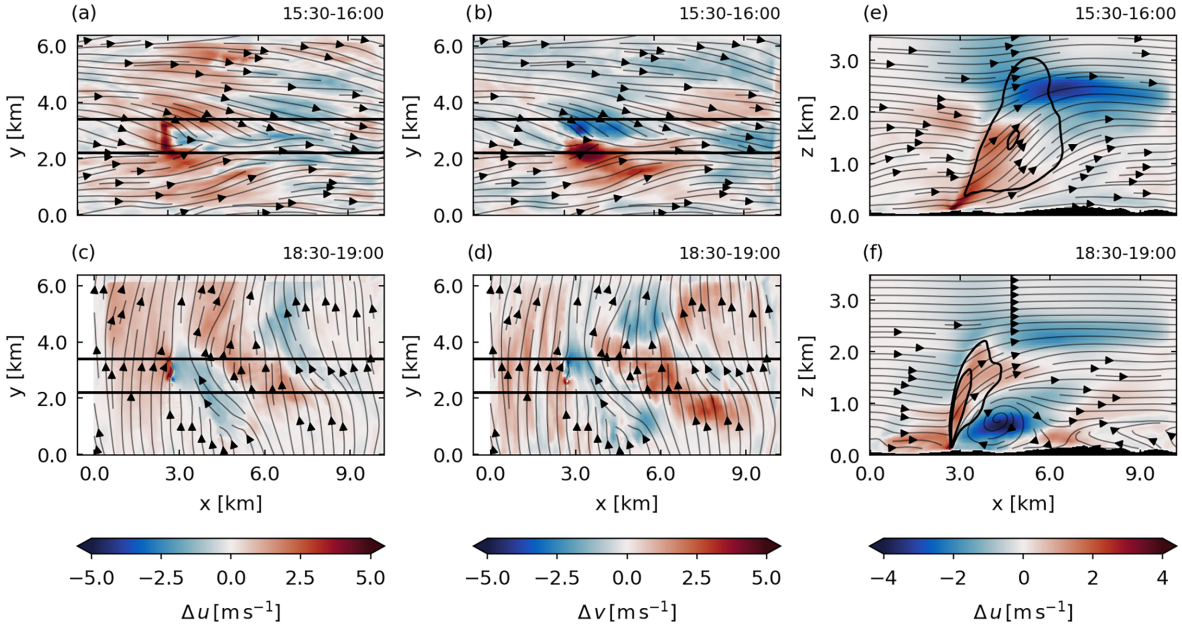

FIGURE 9 Same as Figure 8, but now showing the difference between the *nomeso* and *nomeso_nofire* simulations.

have seen in Figures 2d and 3c that the wind direction near the surface changes from westerly to southwesterly for the *base* simulation. In Figure 8a,b, we consider the half-hourly averaged horizontal (*xy*) flow field and the u (zonal wind) and v (meridional wind) anomaly, respectively, at 100 m above the surface, before the front has passed. Figure 8c,d shows the same anomalies after the front has passed. The anomaly is the difference between the *base* and *base_nofire* simulations.

Before the front, the wind blows perpendicular to the line source (Figure 8a,b). The flow is accelerated upwind of the plume (darker red) and decelerated downwind of the plume (darker blue). In addition, the flow lines converge downwind of the source. After the front, the wind blows at an angle from the southwest on the line source (Figure 8c,d). In contrast to the situation before the front, there is a stronger and more domain-wide acceleration and deceleration area of the wind at this height above the source. The opposite is true for the anomaly in meridional wind Δv, where we see a less localised anomaly before the front as opposed to after. The convergence pattern towards the plume thus changes with the backing of the wind and shows an opposite effect for the zonal and meridional winds.

Figure 8e,f shows a zonal cross-section of the anomaly in zonal wind Δu before and after the front, respectively. The black contours show the vertical velocity. Here we see how, after the front has passed, the plume rises more steeply and reaches larger vertical velocities. We also observe a downward flow downwind of the plume, resulting in a rotor-like circulation. This circulation is due to the reversal of the flow evident from the negative anomaly in Δu (which we also see in Figure 8c). Such downwind flow reversal under strong convective ascent has been noted before in observations (Roberts *et al.*, 2024) and simulations (Peace *et al.*, 2015). However, what is particular about this result is that we can link it directly with the arrival of the front.

We expect that the backing of the wind near the surface plays an important role in the development of this circulation, in addition to the stronger overall convergence. Before the front, the wind blows from the west at nearly all levels (see Figure 3c). In other words, there is little directional wind shear. After the front, the wind blows from the southwest at the surface (Figure 8b), but still from the west higher up. This means that the plume can still be seen to move eastward with the wind in Figure 8f. However, near the surface, the wind now blows more in the meridional direction and the convergence becomes stronger in the zonal direction. The circulation somewhat resembles that of secondary flows (Anderson *et al.*, 2015), where circulations form normal to the mean flow over a heterogeneously heated boundary layer (of which our wildfire can be thought of as an extreme version).

This hypothesis is strengthened when we consider the *nomeso* simulation (Figure 9). Compared with the *base* simulation, the simulation without the mesoscale results in straighter flow lines. As shown before, the change in wind direction before (Figure 9a,b) and after (Figure 9c,d) the front is stronger. Although the general behaviour is the same between the two simulations, we now see a more pronounced downwind circulation (from Figure 9e–f). At the same time, we do not see a clear increase in convergence towards the plume and the Δu anomaly is even

somewhat weaker in the *nomeso* simulation (shown in Appendix B). In addition, the plume in the *nomeso* simulation shows a stronger tilt, similar to the results of Kochanski *et al.* (2013a), who also linked this to low-level wind shear. We therefore attribute the stronger circulation to the increased wind shear, as opposed to stronger convergence. However, testing this hypothesis fully will require (idealised) sensitivity experiments, which also include a fire front that is responsive to the change in wind direction.

The circulations of Figure 9b,d resemble those of Roelofs *et al.* (2026), which correspond to the same simulated period. We find the same results in terms of wind direction and downwind circulation. Our simulations, however, show that this wind field and the downwind circulation are closely tied to the moisture boundary and that there are clear differences between a simulation that includes a mesoscale simulation and one that does not. With the mesoscale nesting, we simulate a lesser degree of wind backing, which is in line with the observations (Figure 2d) and results in a weaker downwind circulation.

4 | CONCLUSION

We have presented a set of mesoscale–microscale simulations to study the interaction between a pyroconvective wildfire plume and a moisture front that occurred during the Santa Coloma de Queralt wildfire. The hypothesis was that the addition of a simulation that resolves mesoscale atmospheric motions would affect the characteristics of pyroconvection. We have indeed found distinct differences between our simulations with and without this mesoscale nesting. The main findings of this research are the following.

- The LES that is nested in the mesoscale model produces a sharp low-level front of enhanced moisture and backing winds, whereas the LES without the mesoscale nesting produces a more gradual increase in moisture.
- The difference in representation of this front influences the timing of overshooting pyrocumulus clouds. In the *base* simulation, the formation of these clouds is directly linked to the arrival of the front. However, because this arrival is simulated too early, the pyrocumulus formation is also simulated too early (1730 UTC as opposed to 1830 UTC). The *nomeso* simulation also produces pyrocumulus clouds, but only after the boundary layer has moistened sufficiently (at 1930 UTC).
- The moisture front modulates the plume circulation. After the passing of the front, we observe a downwind circulation and a more tilted plume, which is more pronounced in the *nomeso* simulation. We hypothesise that the reason for this is the stronger directional wind shear in this simulation.
- We did not find any substantial differences between the simulations in the vertical profiles of potential temperature and specific humidity, compared with the observed in-plume radiosounding.

The radiosounding released during the wildfire provides valuable insight into the thermodynamics associated with pyroconvection. However, the small number of profiles limits a quantitative comparison of the model output with the observations. As the use of these in-plume radiosoundings is becoming more common, forthcoming projects could therefore be directed toward gathering a larger number of radiosoundings from a single extreme wildfire event, thereby improving the robustness of the analysis. In addition, we argue that future modelling efforts should move beyond single case studies and focus on which physical mechanisms connecting pyroconvection and wildfires are shared among extreme wildfire events and which mechanisms result from mesoscale weather effects.

Overall, our research has demonstrated that mesoscale weather effects can influence pyroconvective behaviour considerably and that dedicated mesoscale–microscale modelling can be used to understand these processes in detail. Crucially, resolving the mesoscale influences the timing of pyroconvection, while the effect on plume characteristics is less pronounced. Additionally, our study highlights the potential value of high-resolution weather forecasts, which can resolve mesoscale processes, in wildfire management.

ACKNOWLEDGMENTS

C. van Heerwaarden and T. Roelofs received funding from the Union Civil Protection Mechanism of the European Union under grant agreement no. 101140363 (EWED). Views and opinions expressed are, however, those of the authors only and do not necessarily reflect those of the European Union or the European Commission–EU. Neither the European Union nor the granting authority can be held responsible for them.

CONFLICT OF INTEREST STATEMENT

The authors declare no conflicts of interest.

DATA AVAILABILITY STATEMENT

The data that support the findings of this study are openly available at: Zenodo/KoenvanderAa. All data and code used for the preparation of this article can be found through the Zenodo repository accompanying this article: https://doi.org/10.5281/zenodo.17691211.

ENDNOTES

[1]wildfiredataportal.eu/fire/santa-coloma-de-queralt.
[2]Data are available through wildfiredataportal.eu/fire/santa-coloma-de-queralt.

ORCID

Koen van der Aa https://orcid.org/0009-0000-0612-7289
Bernard Postema https://orcid.org/0009-0007-8498-5490

REFERENCES

Anderson, W., Barros, J.M., Christensen, K.T. & Awasthi, A. (2015) Numerical and experimental study of mechanisms responsible for turbulent secondary flows in boundary layer flows over spanwise heterogeneous roughness. *Journal of Fluid Mechanics*, 768, 316–347. Available from: https://doi.org/10.1017/jfm.2015.91

Ayat, H., Lane, T.P., Wales, S., Reeder, M.J. & Huang, Y. (2025) Rapid surface drying during the black summer bushfires in Australia: Insights from high-resolution simulations. *Journal of Geophysical Research: Atmospheres*, 130, e2024JD041706. Available from: https://doi.org/10.1029/2024JD041706

Baas, P., Verzijlbergh, R., van Dorp, P. & Jonker, H. (2023) Investigating energy production and wake losses of multi-gigawatt offshore wind farms with atmospheric large-eddy simulation. *Wind Energy Science*, 8, 787–805. Available from: https://doi.org/10.5194/wes-8-787-2023

Badlan, R.L., Lane, T.P., Mills, G.A. & Caine, S. (2012) Mesoscale modelling of two drying events: governing processes and implications for fire danger. *Australian Meteorological and Oceanographic Journal*, 62, 143–156. Available from: https://doi.org/10.1071/ES12020

Badlan, R.L., Sharples, J.J., Evans, J.P. & McRae, R.H.D. (2021a) Factors influencing the development of violent pyroconvection. Part I: fire size and stability. *International Journal of Wildland Fire*, 30, 484–497. Available from: https://doi.org/10.1071/WF20040

Badlan, R.L., Sharples, J.J., Evans, J.P. & McRae, R.H.D. (2021b) Factors influencing the development of violent pyroconvection. Part II: fire geometry and intensity. *International Journal of Wildland Fire*, 30, 498–512. Available from: https://doi.org/10.1071/WF20041

Bakhshaii, A. & Johnson, E.A. (2019) A review of a new generation of wildfire–atmosphere modeling. *Canadian Journal of Forest Research*, 49, 565–574. Available from: https://doi.org/10.1139/cjfr-2018-0138

Barnes, C., Madakumbura, G., Abatzoglou, J., Williams, P., Aghakhouchak, A., Pinto, I. et al. (2025) Climate change increased the likelihood of wildfire disaster in highly exposed Los Angeles area.

Bedoya-Valestt, S., Azorin-Molina, C., Gimeno, L., Guijarro, J.A., Sanchez-Morcillo, V.J., Aguilar, E. et al. (2023) Opposite trends of sea-breeze speeds and gusts in eastern Spain, 1961–2019. *Climate Dynamics*, 60, 2847–2869. Available from: https://doi.org/10.1007/s00382-022-06473-0

Bieringer, P.E., Piña, A.J., Lorenzetti, D.M., Jonker, H.J.J., Sohn, M.D., Annunzio, A.J. et al. (2021) A graphics processing unit (GPU) approach to large eddy simulation (LES) for transport and contaminant dispersion. *Atmosphere*, 12, 890. Available from: https://doi.org/10.3390/atmos12070890

Bowman, D.M.J.S. & Sharples, J.J. (2023) Taming the flame, from local to global extreme wildfires. *Science*, 381, 616–619. Available from: https://doi.org/10.1126/science.adi8066

Byram, G.M. (1959) Combustion of forest fuels. In: K. P. Davis (Ed.) *Forest Fire: Control and Use*. New York: McGraw-Hill, pp. 61–89.

Campos, C., Couto, F.T., Filippi, J.B., Baggio, R. & Salgado, R. (2023) Modelling pyro-convection phenomenon during a mega-fire event in Portugal. *Atmospheric Research*, 290, 106776. Available from: https://doi.org/10.1016/j.atmosres.2023.106776

Canadell, J.G., Meyer, C.P.M., Cook, G.D., Dowdy, A., Briggs, P.R., Knauer, J. et al. (2021) Multi-decadal increase of forest burned area in Australia is linked to climate change. *Nature Communications*, 12, 6921. Available from: https://doi.org/10.1038/s41467-021-27225-4

Castellnou, M., Bachfischer, M., Guarque, P., Estivill, L., Bover, M.M., Ruiz, B. et al. (2025) Integrating fireline observations to characterize fire plumes during pyroconvective extreme wildfire events: implications for firefighter safety and plume modeling. *Atmospheric Measurement Techniques*, 18, 7805–7831. Available from: https://doi.org/10.5194/amt-18-7805-2025

Castellnou, M., Bachfischer, M., Miralles, M., Ruiz, B., Stoof, C.R. & de Arellano, J. (2022) Pyroconvection classification based on atmospheric vertical profiling correlation with extreme fire spread observations. *Journal of Geophysical Research: Atmospheres*, 127, e2022JD036920. Available from: https://doi.org/10.1029/2022JD036920

Coen, J.L., Cameron, M., Michalakes, J., Patton, E.G., Riggan, P.J. & Yedinak, K.M. (2013) Wrf-fire: coupled weather–wildland fire modeling with the weather research and forecasting model. *Journal of Applied Meteorology and Climatology*, 52, 16–38. Available from: https://doi.org/10.1175/JAMC-D-12-023.1

Couto, F.T., Filippi, J.B., Baggio, R., Campos, C. & Salgado, R. (2024) Numerical investigation of the pedrógão grande pyrocumulonimbus using a fire to atmosphere coupled model. *Atmospheric Research*, 299, 107223. Available from: https://doi.org/10.1016/j.atmosres.2024.107223

Cunningham, C.X., Williamson, G.J. & Bowman, D.M.J.S. (2024) Increasing frequency and intensity of the most extreme wildfires on earth. *Nature Ecology & Evolution*, 8, 1420–1425. Available from: https://doi.org/10.1038/s41559-024-02452-2

Cunningham, P. (2007) Idealized numerical simulations of the interactions between buoyant plumes and density currents. *Journal of the Atmospheric Sciences*, 64, 2105–2115. Available from: https://doi.org/10.1175/JAS3947.1

Eghdami, M., Juliano, T.W., Jiménez, P.A., Kosovic, B., Castellnou, M., Kumar, R. et al. (2023) Characterizing the role of moisture and smoke on the 2021 Santa Coloma De Queralt pyroconvective event using WRF-fire. *Journal of Advances in Modeling Earth Systems*, 15, e2022MS003288. Available from: https://doi.org/10.1029/2022MS003288

Filippi, J.B., Bosseur, F., Mari, C. & Lac, C. (2018) Simulation of a large wildfire in a coupled fire-atmosphere model. *Atmosphere*, 9, 218. Available from: https://doi.org/10.3390/atmos9060218

Filippi, J.B., Bosseur, F., Mari, C., Lac, C., Moigne, P.L., Cuenot, B. et al. (2009) Coupled atmosphere-wildland fire modelling. *Journal of Advances in Modeling Earth Systems*, 1, 11. Available from: https://doi.org/10.3894/JAMES.2009.1.11

Finney, M.A., McAllister, S.S., Forthofer, J.M. & Grumstrup, T.P. (2021) *Wildland Fire Behaviour: Dynamics, Principles and Processes*. Clayton South: CSIRO Publishing.

Fromm, M., Lindsey, D.T., Servranckx, R., Yue, G., Trickl, T., Sica, R. et al. (2010) The untold story of pyrocumulonimbus. *Bulletin of the American Meteorological Society*, 91, 1193–1210. Available from: https://doi.org/10.1175/2010BAMS3004.1

Fromm, M., Servranckx, R., Stocks, B.J. & Peterson, D.A. (2022) Understanding the critical elements of the pyrocumulonimbus storm sparked by high-intensity wildland fire. *Communications Earth and Environment*, 3, 243. Available from: https://doi.org/10.1038/s43247-022-00566-8

Hanley, D.E., Cunningham, P. & Goodrick, S.L. (2013) Interaction between a Wildfire and the Sea-Breeze Front. In: Qu, J.J., Sommers, W.T., Yang, R., Riebau, A.R. (Eds.) *Remote Sensing and Modeling Applications to Wildland Fires*. Berlin, Heidelberg: Springer, pp. 81–98. Available from: https://doi.org/10.1007/978-3-642-32530-4_7

Hersbach, H., Bell, B., Berrisford, P., Hirahara, S., Horányi, A., Muñoz-Sabater, J. et al. (2020) The era5 global reanalysis. *Quarterly Journal of the Royal Meteorological Society*, 146, 1999–2049. Available from: https://doi.org/10.1002/qj.3803

Heus, T., van Heerwaarden, C.C., Jonker, H.J.J., Siebesma, A.P., Axelsen, S., van den Dries, K. et al. (2010) Formulation of the Dutch atmospheric large-eddy simulation (dales) and overview of its applications. *Geoscientific Model Development*, 3, 415–444. Available from: https://doi.org/10.5194/gmd-3-415-2010

Jones, M.W., Kelley, D.I., Burton, C.A., Giuseppe, F.D., Barbosa, M.L.F., Brambleby, E. et al. (2024) State of wildfires 2023–2024. *Earth System Science Data*, 16, 3601–3685. Available from: https://doi.org/10.5194/essd-16-3601-2024

Kochanski, A., Jenkins, M.A., Sun, R., Krueger, S., Abedi, S. & Charney, J. (2013a) The importance of low-level environmental vertical wind shear to wildfire propagation: Proof of concept. *Journal of Geophysical Research: Atmospheres*, 118, 8238–8252. Available from: https://doi.org/10.1002/jgrd.50436

Kochanski, A.K., Jenkins, M.A., Mandel, J., Beezley, J.D. & Krueger, S.K. (2013b) Real time simulation of 2007 Santa Ana fires. *Forest Ecology and Management*, 294, 136–149. Available from: https://doi.org/10.1016/j.foreco.2012.12.014

Lareau, N.P. & Clements, C.B. (2016) Environmental controls on pyrocumulus and pyrocumulonimbus initiation and development. *Atmospheric Chemistry and Physics*, 16, 4005–4022. Available from: https://doi.org/10.5194/acp-16-4005-2016

Luderer, G., Trentmann, J. & Andreae, M.O. (2009) A new look at the role of fire-released moisture on the dynamics of atmospheric pyro-convection. *International Journal of Wildland Fire*, 18, 554–562. Available from: https://doi.org/10.1071/WF07035

Markowski, P. & Richardson, Y. (2010) What is the Mesoscale? In: Markowski, P. & Richardson, Y. (Eds.) *Mesoscale Meteorology in Midlatitudes*. Chichester: John Wiley & Sons, Ltd, pp. 3–10. Available from: https://doi.org/10.1002/9780470682104.ch1

Miller, S.T., Keim, B.D., Talbot, R.W. & Mao, H. (2003) Sea breeze: structure, forecasting, and impacts. *Reviews of Geophysics*, 41, 2003RG000124. Available from: https://doi.org/10.1029/2003RG000124

Nolan, R.H., Boer, M.M., Collins, L., de Dios, V., Clarke, H., Jenkins, M. et al. (2020) Causes and consequences of eastern Australia's 2019–20 season of mega-fires. *Global Change Biology*, 26, 1039–1041. Available from: https://doi.org/10.1111/gcb.14987

Peace, M., Mattner, T., Mills, G., Kepert, J. & McCaw, L. (2015) Fire-modified meteorology in a coupled fire–atmosphere model. *Journal of Applied Meteorology and Climatology*, 54, 704–720. Available from: https://doi.org/10.1175/JAMC-D-14-0063.1

Peterson, D.A., Hyer, E.J., Campbell, J.R., Solbrig, J.E. & Fromm, M.D. (2017) A conceptual model for development of intense pyrocumulonimbus in Western North America. *Monthly Weather Review*, 145, 2235–2255. Available from: https://doi.org/10.1175/MWR-D-16-0232.1

Pinto, P., Silva, Á., Viegas, D.X., Almeida, M. & Ribeiro, L.M. (2022) *Influence of a sea-breeze front over a fire plume, Pedrogão Grande wildfires (20 June 2017) 264-272*.

Postema, B., Heerwaarden, C.V., Stratum, B.V., Dorp, P.V., Baas, P. & Jonker, H. (2026) Simulating the year to minute wind spectrum with mesoscale coupled large eddy simuations. *Quarterly Journal of the Royal Meteorological Society*, e70147. Available from: https://doi.org/10.1002/qj.70147

Postema, B., Verzijlbergh, R.A., van Dorp, P., Baas, P. & Jonker, H.J.J. (2025) Estimating long-term annual energy production from shorter-time-series data: methods and verification with a 10-year large-eddy simulation of a large offshore wind farm. *Wind Energy Science*, 10, 1471–1484. Available from: https://doi.org/10.5194/wes-10-1471-2025

Potter, B.E. (2012) Atmospheric interactions with wildland fire behaviour – II. plume and vortex dynamics. *International Journal of Wildland Fire*, 21, 802–817. Available from: URL 10.1071/WF11129

Potter, B.E. & Anaya, M.A. (2015) A wildfire-relevant climatology of the convective environment of the united states. *International Journal of Wildland Fire*, 24, 267–275. Available from: https://doi.org/10.1071/WF13211

Roberts, M., Lareau, N.P., Juliano, T.W., Shamsaei, K., Ebrahimian, H. & Kosovic, B. (2024) Sensitivity of simulated fire-generated circulations to fuel characteristics during large wildfires. *Journal of Geophysical Research: Atmospheres*, 129, e2023JD040548. Available from: https://doi.org/10.1029/2023JD040548

Roelofs, T., Castellnou, M., de Arellano, J., Janssens, M., van Heerwaarden, C. & Tristanroelofs, T.R. (2026) Wildfire-atmosphere interactions during the santa coloma de queralt fire: the development of a fire-induced circulation (preprint). *Atmospheric Chemistry and Physics*. Available from: https://doi.org/10.5194/egusphere-2025-4620

Rozema, W., Bae, H.J., Moin, P. & Verstappen, R. (2015) Minimum-dissipation models for large-eddy simulation. *Physics of Fluids*, 27, 85107. Available from: https://doi.org/10.1063/1.4928700

Schalkwijk, J., Griffith, E.J., Post, F.H. & Jonker, H.J.J. (2012) High-performance simulations of turbulent clouds on a desktop pc: Exploiting the GPU. *Bulletin of the American Meteorological Society*, 93, 307–314. Available from: https://doi.org/10.1175/BAMS-D-11-00059.1

Schalkwijk, J., Jonker, H.J.J., Siebesma, A.P. & Meijgaard, E.V. (2015) Weather forecasting using GPU-based large-eddy simulations. *Bulletin of the American Meteorological Society*, 96, 715–723. Available from: https://doi.org/10.1175/BAMS-D-14-00114.1

Schepers, G., van Dorp, P., Verzijlbergh, R., Baas, P. & Jonker, H. (2021) Aeroelastic loads on a 10-mw turbine exposed to extreme

events selected from a year-long large-eddy simulation over the north sea. *Wind Energy Science*, 6, 983–996. Available from: https://doi.org/10.5194/wes-6-983-2021

Sofiev, M., Ermakova, T. & Vankevich, R. (2012) Evaluation of the smoke-injection height from wild-land fires using remote-sensing data. *Atmospheric Chemistry and Physics*, 12, 1995–2006. Available from: https://doi.org/10.5194/acp-12-1995-2012

Tedim, F., Leone, V., Amraoui, M., Bouillon, C., Coughlan, M.R., Delogu, G.M. et al. (2018) Defining extreme wildfire events: Difficulties, challenges, and impacts. https://api.semanticscholar.org/CorpusID:156054450

Troen, I.B. & Mahrt, L. (1986) A simple model of the atmospheric boundary layer; sensitivity to surface evaporation. *Boundary-Layer Meteorology*, 37, 129–148. Available from: https://doi.org/10.1007/BF00122760

Turco, M., Jerez, S., Augusto, S., Tarín-Carrasco, P., Ratola, N., Jiménez-Guerrero, P. et al. (2019) Climate drivers of the 2017 devastating fires in portugal. *Scientific Reports*, 9, 13886. Available from: https://doi.org/10.1038/s41598-019-50281-2

van Stratum, B.J.H., van Heerwaarden, C.C. & de Arellano, J. (2023) The benefits and challenges of downscaling a global reanalysis with doubly-periodic large-eddy simulations. *Journal of Advances in Modeling Earth Systems*, 15, e2023MS003750. Available from: https://doi.org/10.1029/2023MS003750

Wilke, D.J., Kepert, J.D. & Tory, K.J. (2022) The meteorology of the tathra bushfire. *Weather and Forecasting*, 37, 581–600. Available from: https://doi.org/10.1175/WAF-D-21-0084.1

How to cite this article: van der Aa, K., Postema, B., van Heerwaarden, C., Roelofs, T. & Jonker, H. (2026) The role of mesoscale weather effects in simulating pyroconvection: A case study of the Santa Coloma de Queralt wildfire. *Quarterly Journal of the Royal Meteorological Society*, e70227. Available from: https://doi.org/10.1002/qj.70227

APPENDIX A. ZONAL CROSS-SECTIONS

Figure A1 shows the zonal cross-sections corresponding to the meridional cross-sections of Figure 6. Figure A1a–c shows the evolution of the moisture (shaded) and vertical velocity (contours) for the *base* simulation, while Figure A1d–f shows this for the *nomeso* simulation. The white lines show the area over which the cross-sections of Figure 6 are averaged. This illustrates that, after the front has passed, the plume becomes steeper and moves into the area over which we average. The figure shows that it is complex to find an averaging window that is not too wide but still captures all the essential characteristics.

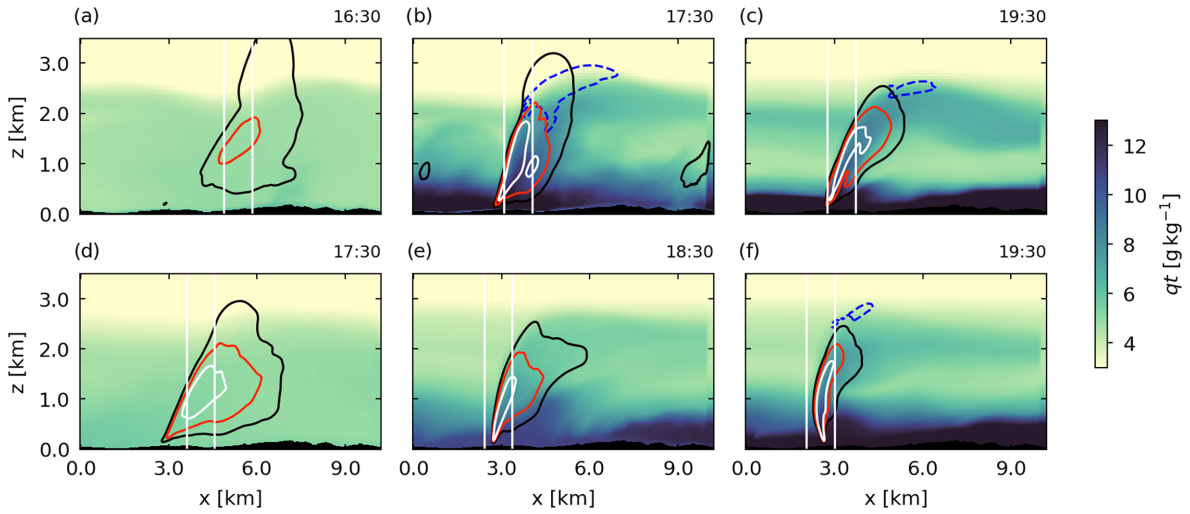

FIGURE A1 Similar to Figure 6, but now showing zonal (*xz*) cross-sections. Additionally, the white lines show the area over which the meridional (*yz*) cross-sections in Figure 6 are averaged.

APPENDIX B. ADDITIONAL VERTICAL PROFILES

Figure B1a,b shows the sensitivity to our definition of the plume of the vertical profiles of potential temperature for the *base* and *nomeso* simulations, respectively. These figures show that the w threshold that is used influences the lower kilometre of the profile substantially, in accordance with the large variability shown in Figure 5b. In contrast, the variation in the qt profiles for different thresholds is negligible (not shown).

Figure B1c shows the time evolution of the vertical profiles of the horizontal wind anomaly downwind of the plume over time. The blue lines represent the time evolution of the *base* simulation and the red line that of the *nomeso* simulation. The location of the vertical profiles corresponds to the location of the observed downwind circulation. This figure shows that the *base* simulation has larger horizontal wind-speed anomalies near the surface, but the *nomeso* simulation has larger anomalies between 500 and 1000 m.

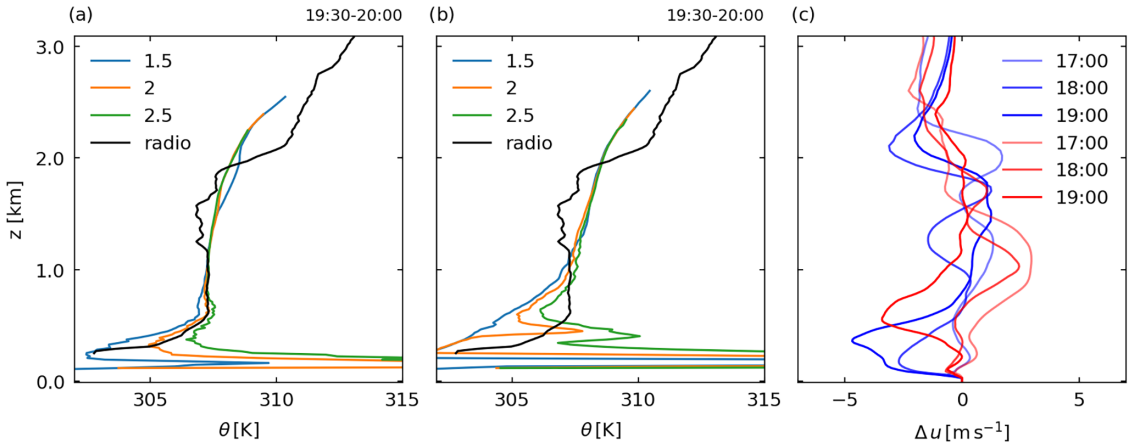

FIGURE B1 (a) *Base* simulation vertical profiles of potential temperature θ in the plume based on three different definitions for the plume ($w = 1.5, 2.0, 2.5$), as coloured lines. The black line shows the vertical profile measured by the radiosounding (the same as in Figure 5b). (b) Same as in (a), but for the *nomeso* simulation. (c) Vertical profiles of the anomaly in horizontal wind speed downwind of the plume at three different times (1700, 1800, 1900 UTC) for the *base* (blue) and *nomeso* simulations. The location of the vertical profile corresponds to the location of the downwind circulation observed in Figures 8f and 9f.